DEVELOPMENT OF SILICON BASED COMPACT OPTOMECHANICAL ACCELEROMETERS

A Thesis

by

BRINA BIANCA MARTINEZ

Submitted to the Graduate and Professional School of
Texas A&M University
in partial fulfillment of the requirements for the degree of

MASTER OF SCIENCE

Chair of Committee,	Felipe Guzmán
Committee Members,	Jose Sanjuan Munoz
	Chandler Benjamin
Head of Department,	Ivett A. Leyva

May 2023

Major Subject: Aerospace Engineering

Copyright 2023 Brina Bianca Martinez

ABSTRACT

High-sensitivity accelerometers are a key technology in many applications including gravitational physics such as ground-based gravitational wave (GW) detectors [1], gravimetry measurements, vibration noise detection, inertial navigation systems, and many more. Highly sensitive inertial sensors that are commercially available are often large and incompatible with vacuum and cryogenic environments. The commercially available sensors that are compact in size face the issues of high acceleration noise floors. Fused silica has demonstrated high mechanical quality factors (Q) at room temperature, roughly 10^7. However at 110 K the Q drops to 10^4 and at cryogenic temperatures ($\sim$20 K) it drops even further to 10^3 [2]. Silicon exhibits significantly better performance across both cryogenic and room temperatures, between 10^7 and 10^8 respectively [2, 3]. This is relevant for future ground-based gravitational wave detectors where cryogenic environments will be used to improve the sensitivity of the observatories [4, 5]. We will investigate compact millimeter-scale resonators made of silicon.

This thesis covers the development of compact optomechanical accelerometers optimized for frequencies at and below 1 kHz with comparable or enhanced acceleration noise floors. This includes the design, modeling, and fabrication of monolithic mechanical resonators, and their integration with laser interferometers to read out their test mass dynamics under the presence of external accelerations.

DEDICATION

To my mother, Olivia.

Thank you for your love, support, and never-ending belief in me.

To my father, Saul.

Thank you for your love, and support, and for teaching me that I could achieve any goal I set.

To my sisters Brittney and Briana.

For being my best friends and for always inspiring me to do more.

ACKNOWLEDGMENTS

To Dr. Felipe Guzmán. Thank you for your unwavering support as a research advisor; for being optimistic, passionate, and a motivational leader; for believing in my capabilities even when others did not.

To Dr. Jose Sanjuan. Thank you for your support and guidance through this research; for your enthusiasm and a never-ending supply of knowledge; for asking the questions I would have never thought to ask myself; for being a wonderful mentor.

To Dr. Chandler Benjamin. Thank you for being one of the best professors I have ever had; for your patience and generosity; for pushing me to set my goals even higher; for believing in what I could achieve.

To Dr. Mario Diaz. Thank you for giving me my first-ever opportunity to do research as an undergrad; for continuing to support me now and wherever I go in my academic journey.

To Lee Ann Capistran. Thank you for joining me through many of my academic journeys so far; for being my hotel roommate at many conferences and my roommate through grad school; for being a tourist with me wherever we go; for being my partner in research; for the endless laughs and inside jokes; for always believing in me; for being my best friend.

To Dr. Guillermo Valdés. Thank you for guiding me as an undergraduate student to now; for your advice in both research and life; for being a great mentor and friend.

To Alberto Zamora Mendieta. Thank you for the countless hours of being my tutor and the late-night study sessions; for always reminding me of what I can accomplish; for being a wonderful friend.

To Andrea Nelson. Thank you for always letting me rant over my ideas regarding this research; for your guidance and helping me get through the obstacles in this research; for reviewing each paper I've written; for the fun chats regarding anime and other pop culture; for being the kindest person I have ever met; for being an amazing friend.

To Dr. Xiangyu Guo. Thank you for all the help on this research in the lab; for the boba tea and coffee trips; for reviewing all my papers; for your excitement and patience; for being a great friend.

To Edoardo Dalla Ricca. Thank you for teaching me so much about Italy and what good pizza and pasta are like; for the daily coffee breaks; for the laughter and liveliness you brought with you every day; for encouraging me to live life to the fullest; for being a good friend.

To Pengzhuo Wang and Dr. Adam Hines. Thank you for all the guidance and advice on this research in the labs and for being great friends.

To all the other friends I have made here at Texas A&M. Ian Harley-Trochimczyk, Jackson Dahn, Mohanad Warrayat, Keith Hunter, Dr. Yanqi Zhang, Grigory Nikitin, Giorgi Gvasalia, David Van Wijk, Yalan Shu, Alex Salinas, Lucia Lang, Julie Shafer, and Conrad Su. Thank you for your friendship, and for making even the most boring days fun.

To my friends back home. Wendy Mendoza, Victor Perez, Richard Camuccio, Moises Castillo, Samantha Martinez, Wahltyn Rattray, Victor De Los Santos, and Tanya Llanas. Thank you for the knowledge you have given me since the beginning of my academic career; for the support, and motivation, and for your friendship; for bringing me joy from far away.

To my dog Kenma. For bringing me happiness, emotional comfort, and unconditional love.

Finally, I would like to thank everyone else who has joined me on this journey so far, the aerospace department faculty and staff, and the staff at Aggiefab for making my time at Texas A&M University wonderful.

CONTRIBUTORS AND FUNDING SOURCES

Contributors

This work was supported by a thesis committee consisting of Professors Dr. Felipe Guzmán and Dr. Jose Sanjuan of the Department of Aerospace Engineering and Dr. Chandler Benjamin of the Department of Mechanical Engineering.

The monolithic mechanical parallelogram resonator presented in Chapter 1.1 was developed by Professor Felipe Guzmán and was further developed in collaboration with Andrea Nelson.

Guidance regarding the properties of the watt-linkage system for the mechanical pendulum resonator was provided by Dr. Joris van Heijningen, Dr. Eric Hennes, and Dr. Alessandro Bertolini.

Guidance on the optical readout setup and data processing has been provided by Dr. Xiangyu Guo, Dr. Guillermo Valdés, Dr. Jose Sanjuan, Pengzhuo Wang, and Andrea Nelson.

Assistance in developing the aluminum mount described in Chapter 2.5 was given by Jonathan Mock.

Advice on using the multiphysics software in this project was also given by Andrea Nelson and Dr. Adam Hines.

All other work conducted for the thesis was completed by the student independently.

Funding Sources

Graduate study was supported by an assistantship from Dr. Felipe Guzmán along with a fellowship from the Aerospace Engineering Department at Texas A&M University and funding from the National Science Foundation (NSF) (grant PHY-2045579).

TABLE OF CONTENTS

Page

ABSTRACT ii

DEDICATION iii

ACKNOWLEDGMENTS iv

CONTRIBUTORS AND FUNDING SOURCES vi

TABLE OF CONTENTS vii

LIST OF FIGURES ix

LIST OF TABLES xiii

1. INTRODUCTION 1
   - 1.1 Background 1
   - 1.2 Accelerometers 2
     - 1.2.1 Mechanical resonators and Optomechanics 2
   - 1.3 Thesis Outline 5

2. OPTOMECHANICAL ACCELEROMETERS: DESIGN, MODELING, FABRICATION, AND READOUT. 6
   - 2.1 Material characteristics 6
   - 2.2 Mechanical resonator designs 6
   - 2.3 Modeling and analysis 9
   - 2.4 Fabrication method 10
   - 2.5 Optical Readout 16

3. RESULTS 19
   - 3.1 Modeling results 19
   - 3.2 Fabrication 21
     - 3.2.1 Parallelogram resonator 21
     - 3.2.2 Pendulum resonator 21
   - 3.3 Fabricated fused silica pendulum resonator 22
   - 3.4 Optical Read-out 23

4. CONCLUSION 30

4.1 Future work 30

REFERENCES 32

LIST OF FIGURES

FIGURE Page

1.1 The transfer function of external acceleration to the resonator's test mass displacement. This plot is in regard to the silicon pendulum resonator discussed in Figure 2.1a. This transfer function shows us that the frequencies above the fundamental frequency of the resonator do not couple well into the test mass motion. Below resonance, vibrations are coupled into the test mass motion. 4

2.1 (a) Geometry of our silicon pendulum resonator generated in Solidworks. This version of the resonator has overall dimensions of 30 mm×30 mm×380 μm, and a mass of 0.71 g. The test mass is roughly 0.47 g and is supported by two flexures with a thickness of roughly 141 μm. and (b) Geometry of our silicon parallelogram resonator generated in Solidworks. This version of the resonator has overall dimensions of 15 mm×10 mm×280 μm, and a mass of 72.5 mg. The test mass is roughly 5.4 mg and is supported by two flexures with a thickness of roughly 120 μm. From these models, we can calculate the mechanical properties of the resonators including the fundamental frequency and maximum stress. 8

2.2 Geometry of our fused silica optomechanical pendulum resonator generated in Solidworks. From this model, we can calculate the mechanical properties of our resonator including the fundamental frequency and maximum stress. This version of the resonator has overall dimensions of 30 mm×30 mm×500 μm, and a mass of 0.95 g. The test mass is roughly 0.59 g and is supported by two flexures with a thickness of roughly 95 μm at the thinner portions and 235 μm at the thicker portions. 9

2.3 A Solidworks simulation of the fundamental mode of the pendulum and parallelogram resonator. The blue color signifies a static area while the red, green, yellow, and orange signify the different amplitudes of the moving parts. The displacement of the test mass in these simulations is exaggerated to show the motion. The expected displacement of the test masses with a force of gravity at 9.8 m/s^2 is shown in Figure 2.4 11

2.4 A Solidworks simulation of the fundamental mode of the pendulum and parallelogram resonator. The blue color signifies a static area while the red, green, yellow, and orange signify the different amplitudes of the moving parts. The displacement of the test mass in these simulations is to a scale of 1 to show the expected displacement of the test masses with a force of gravity at 9.8 m/s^2. 11

2.5 A zoomed view of a section from a Solidworks simulation of the stress across the pendulum resonator. The maximum stress on the body will always be where the flexures connect to the frame and test mass. The red signifies the area with the maximum stress while the blue signifies the areas with the minimum stress. As shown on the color bar, the yield strength for silicon is 120 MPa and the maximum stress seen in this simulation is roughly 14.31 MPa. 12

2.6 The finalized designs of the resonators created in a photomask for performing photolithography. The photomask for the parallelogram has multiple versions of the resonator with varying flexure sizes. 12

2.7 The sizes of the silicon wafers we use to fabricate our resonators are often larger than the size of our resonator. By cutting the wafers into smaller pieces we can fabricate multiple resonators using a single wafer. 13

2.8 The silicon pieces are coated with a layer of aluminum. The aluminum acts as a selective hard mask for the remainder of the fabrication process. This aluminum can be easily removed after fabrication using an aluminum etchant. 13

2.9 A layer of photoresist is applied above the aluminum. As seen in the images above the different colors on the sample represent the varying thickness of the photoresist. When exposed to light the photoresist is selectively weakened and can be washed away using a developer, leaving the lightly shown pattern of the resonator. 14

2.10 Before removing the photoresist, an aluminum etchant is used to remove the exposed areas of aluminum. Once the aluminum is etched we remove any remaining photoresist and are left with a dark pattern in the leftover aluminum. The dark areas are the exposed silicon. 15

2.11 To prepare our sample for etching, it needs to be placed onto a carrier wafer. Heat sink paste (shown as dots above) is used to promote anisotropy through thermal conductivity and mount the sample to the carrier wafer so it does not move. 15

2.12 A schematic of the components used to create a Fabry-Pérot system. Laser light at 1550 nm is sent through an isolator, which protects the laser from any reflected light. This is followed by a 50/50 fiber split where one half goes through an optical circulator and the other half goes into a primary photodetector for power normalization. The optical circulator carries the laser light to the resonator which is reflected back through the circulator and carried into a secondary photodetector which records the signal. 17

2.13 A Solidworks assembly of the mount for the pendulum resonator. 18

3.1 (a) Calculated expected linear spectral density of displacement thermal noise floor for a silicon pendulum resonator with a fundamental frequency of 52.4 Hz and 0.47 g test mass at the cryogenic temperature of 20 K and in vacuum, and (b) Calculated expected linear spectral density of acceleration thermal noise for a silicon pendulum resonator with a fundamental frequency of 52.44 Hz and 0.47 g test mass at the cryogenic temperature of 20 K and in vacuum. Also plotted are the contributions from each loss mechanism, from which we can see that surface losses are the dominant noise source for frequencies below resonance followed by thermoelastic losses. The theoretical Q-value for this design is 4.3×10^5 21

3.2 (a) Calculated expected linear spectral density of displacement thermal noise floor for a silicon parallelogram resonator with a fundamental frequency of 1 kHz and 5.4 mg test mass at the cryogenic temperature of 20 K and in vacuum, and (b) Calculated expected linear spectral density of acceleration thermal noise for a silicon parallelogram resonator with a fundamental frequency of 1 kHz and 5.4 mg test mass at the cryogenic temperature of 20 K and in vacuum. Also plotted are the contributions from each loss mechanism, from which we can see that surface losses are the dominant noise source for frequencies below resonance followed by thermoelastic losses. The theoretical Q-value for this design is 3.1×10^5 22

3.3 (a) Calculated expected linear spectral density of displacement thermal noise floor for a fused silica pendulum resonator with a fundamental frequency of 39.44 Hz and 0.59 g test mass at the room temperature of 293 K and in vacuum, and (b) Calculated expected linear spectral density of acceleration thermal noise for a fused silica pendulum resonator with a fundamental frequency of 39.44 Hz and 0.59 g test mass at the room temperature of 293 K and in vacuum. Also plotted are the contributions from each loss mechanism, from which we can see that surface and thermoelastic losses are the dominant noise source for frequencies below resonance. The theoretical Q-value for this design is 3.0568×10^5 23

3.4 (a) The parallelogram resonator pattern is stamped, developed, and has had the aluminum etched away on the patterned sections on two pieces of cut 280 μm silicon wafer. (b) The patterned parallelogram resonator is etched thoroughly through the Cryo-Si process 24

3.5 (a) The pendulum resonator pattern is stamped, developed, and has had the aluminum etched away on the patterned sections on a piece of 380 μm silicon wafer. (b) The patterned pendulum resonator is partially etched through the Cryo-Si process but has issues with the heat sink paste beneath it 24

3.6 A fully fabricated fused silica pendulum resonator. This model used an earlier design where the flexures thinned out toward the ends. The experimental fundamental frequency for this model was roughly 32 Hz and the Q measurement in air was roughly 2,035 25

3.7 An optical flag measurement was utilized to gather a preliminary measurement of the performance of the fully fabricated fused silica pendulum resonator. The experimental fundamental frequency for this model was roughly 32 Hz and the Q measurement in air was roughly 2,035. 26

3.8 The motion recorded from the flag measurement on the fused silica pendulum resonator is shown above. The resonant frequency peak is around 32 Hz. 26

3.9 A compact fused silica resonator with overall dimensions of 20 mm$\times$17 mm$\times$10 mm and a fundamental frequency of roughly 3 kHz. 27

3.10 A low finesse Fabry-Pérot cavity formed along the top of the fused silica 3 kHz resonator test mass and frame. 28

3.11 The Fabry-Pérot setup attached to the 3 kHz resonator. 29

3.12 The fabricated aluminum mount for the pendulum resonator. The inner perimeter of the mount is lined with threaded holes so ball bearings can be placed. A sample resonator frame is shown sitting on top of them. 29

LIST OF TABLES

TABLE Page

3.1 Theoretical fundamental and higher order modes of the silicon pendulum resonator. . 19

3.2 Theoretical fundamental and higher order modes of the silicon parallelogram resonator. 20

3.3 Theoretical fundamental and higher order modes of the fused silica parallelogram resonator. 20

1. INTRODUCTION

1.1 Background

Inertial sensing is a critical capability for applications such as inertial navigation (to estimate trajectories from acceleration measurements) [6], seismic vibration and isolation sensing [1, 7], gravimetry (to measure and correct for non-gravitational forces) [8], and much more. Inertial sensors measure the vibration, orientation, and acceleration of an object with respect to an inertial reference frame.

There are different types of inertial sensors commercially available varying in size, however, many use electrostatic readouts to track motion, such as micro-electromechanical systems (MEMS) [8, 9] which can be found in objects such as smartphones, cars, airplanes, pressure sensors, and many more. The electrostatic readouts, while effective, have resulted in the sensor being affected by the surrounding magnetic field, stray capacitances, and often having high noise floors [10]. The available commercial inertial sensors are also incompatible with operating at cryogenic temperatures and sometimes require alterations around the system so that they are vacuum compatible. The materials and designs that are currently used to produce inertial sensors are often large and heavy, which results in them not being portable or compatible with small spacecraft devices. This is particularly crucial regarding next-generation ground-based gravitational wave (GW) detectors as they plan to continue operation in vacuum and implement cryogenic temperatures to improve their sensitivity by reducing thermal noise fluctuations. The inertial sensors in current ground-based GW detectors are essential for tracking and measuring local seismic noise around the detectors so that they can be correlated, mitigated, or completely removed [1, 11].

Compact optomechanical accelerometers fabricated from fused silica have shown a good agreement in sensitivity in comparison to a large seismometer [12]. Fused silica has a high quality factor, Q, at room temperature, however, it drops significantly at lower temperatures [2, 3]. Studies on the characteristics of silicon have shown that the material maintains a high Q across both room

and low temperatures, making it a candidate material to overcome the issues fused silica faces at cryogenic temperatures.

1.2 Accelerometers

An accelerometer measures the motion of a mass-spring system, which can then be converted to acceleration via Equation 1.4. When the movement of the test mass is recorded, we can reveal the characteristics of the acceleration that caused its motion. An accelerometer is subject to different loss mechanisms contributing to its noise floor. These include thermoelastic losses (bending of the flexures as a result of varying temperatures), bulk losses (energy losses that are natural to the material), and surface losses (losses due to natural imperfections on the surface of the device or from damage such as a scratch), along with gas-damping losses when not in vacuum (due to the frictions of varying gas around the device such as air). To improve the overall noise floor, current commercial accelerometers are developed with large, costly, and heavy characteristics such as large test masses, and are fabricated with a material such as metal, which makes the entire structure large and incompatible with applications that require compact and portable sensors.

1.2.1 Mechanical resonators and Optomechanics

The accelerometers in this thesis will be produced using a monolithically fabricated mechanical resonator combined with an optical readout. The displacement of the test mass on the mechanical resonators will be measured via the method of optomechanics which involves the study and application of optical and mechanical properties. The mechanical resonator consists of an outer frame, a test mass, and two flexures that are parallel. The configurations of the designs change depending on the goals for the overall size, fundamental frequency, and sensitivity. Different fundamental modes result in different motions for the test mass. In this work, we focus on the fundamental mode with linear motion.

The acceleration sensitivity of the optomechanical accelerometers is ultimately limited by their thermal noise floor [13] and the sensitivity of the interferometric readout. Specifically, the mechanical losses of the material, i.e., the so-called mechanical quality factor, Q, is an important

characteristic of the performance of the models. The Q, given by Equation 1.1 [14], describes the energy dissipation mechanisms of the resonator at a given frequency ω_0, where ϕ is the associated loss coefficient. Q can be described as the ratio between the energy stored in the resonator and the energy dissipated through the oscillations it exhibits until it becomes stationary again. A resonator with a high Q is preferred as it means that the oscillations result in small losses of energy per cycle and has a longer decay period than a resonator with a lower Q.

$$Q = \frac{1}{\phi(\omega_0)} = \frac{\omega_0}{\Delta\omega} \tag{1.1}$$

We characterize our resonators as spring-mass-damper systems with an equation of motion given by Equation 1.2 [12], where m is the total mass of the resonator, ω_0 is the angular fundamental frequency, Γ_v is the velocity damping rate, and $\phi(\omega)$ is the internal loss coefficient.

$$F = m\ddot{x} + m\Gamma_v\dot{x} + m\omega_0^2(1 + i\phi(\omega))x \tag{1.2}$$

The thermal motion is described by Equation 1.3, where k_B is the Boltzmann constant, T is the temperature in Kelvin, and ω is the angular frequency. This equation is a complex differential equation however, in this work we use the real part of this solution because of the fluctuation-dissipation theorem explained in [14].

$$x_{th}^2(\omega) = \frac{4k_BT}{m\omega}\frac{\omega\Gamma_v + \omega_0^2\phi(\omega)}{(\omega_0^2 - \omega^2)^2 + (\omega\Gamma_v + \omega_0^2\phi(\omega))^2} \tag{1.3}$$

The test mass on the resonator experiences a certain motion and displacement during its oscillations when external accelerations are applied. To understand what the external accelerations are, we apply a transfer function to characterize the displacement to accelerations. The transfer function relates the input and output properties of the system, in our case the fundamental frequency of the resonator, ω_0, the Q, and the acceleration. The transfer function relating the displacement of the resonator to acceleration is given by Equation 1.4 [14].

$$\frac{x(\omega)}{a(\omega)} = \frac{-1}{\omega_0^2 - \omega + i(\omega\Gamma_v + \omega_0^2\phi(\omega))} \tag{1.4}$$

This equation yields both a real and complex solution. In our calculations, we do consider the imaginary parts. However, in most cases, we can take the magnitude of the complex solution as it is a byproduct of the calculation and does not have a physical meaning. An example of what the transfer function looks like is shown in Figure 1.1. Here the magnitude of the function is taken and shown.

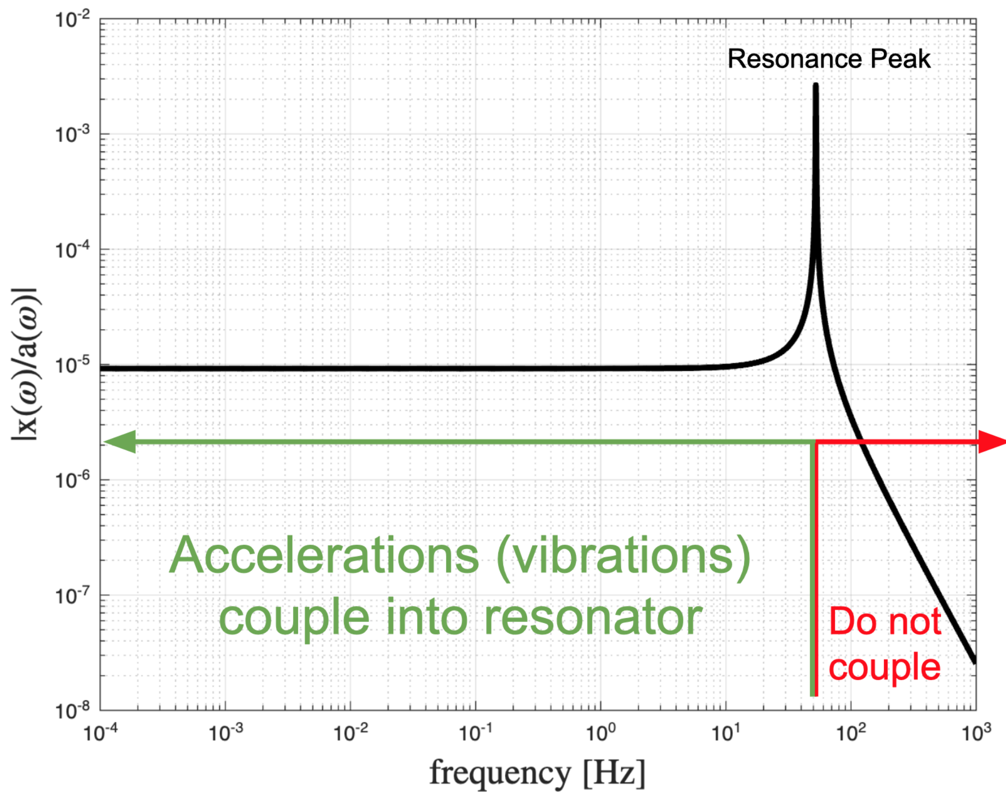

Figure 1.1: The transfer function of external acceleration to the resonator's test mass displacement. This plot is in regard to the silicon pendulum resonator discussed in Figure 2.1a. This transfer function shows us that the frequencies above the fundamental frequency of the resonator do not couple well into the test mass motion. Below resonance, vibrations are coupled into the test mass motion.

Combining Equations 1.3 and 1.4, the thermal acceleration noise is shown by Equation 1.5.

$$a_{th}(\omega) = \sqrt{\frac{4k_BT}{m\omega}(\omega\Gamma_v + \omega_0^2\phi(\omega))} \tag{1.5}$$

From Equation 1.5, we find the noise floor is inversely proportional to mQ/ω_0. To get the best thermal noise floor possible, we have to get the highest possible mQ/ω_0 value for our designs, ultimately increasing the acceleration sensitivity.

For the mechanical resonators in this thesis, an optomechanical accelerometer will be established via a Fabry-Pérot cavity [15, 16], where the cavity length and the resonant wavelength change as the test mass oscillates. The intrinsic transfer function, which converts the test mass motion into acceleration for the system is dependent on the resonator's fundamental frequency, ω_0, and the mechanical Q. As shown in Figure 1.1, for frequencies above the fundamental frequency, accelerations will couple into the resonator motion at $1/\omega^2$. Below the fundamental frequency, the coupling will approach $1/\omega_0^2$.

1.3 Thesis Outline

The contents of this thesis are developed in part from the results of a combination of journal publications [17, 18, 19], and are organized as follows:

- Chapter 2 describes the methods by which we will approach the issues described above. This includes the mechanical resonators we have developed, the material characteristics of our designs, the process in which we have fabricated our resonators, and the optical readout we have developed for our testing.

- Chapter 3 describes the early results we have obtained. This includes the results of the fabrication of our designs, and the results from the operation of our optical readout.

2. OPTOMECHANICAL ACCELEROMETERS: DESIGN, MODELING, FABRICATION, AND READOUT.

In this section, we will discuss the approach to developing the resonators. This includes the materials used, the design, modeling, fabrication, and readout we have established.

2.1 Material characteristics

Since we want our resonators to be compact and portable while maintaining low noise floors we do not want to use a material such as aluminum or titanium. Fused silica has demonstrated high mechanical Q's at room temperatures with both large and compact accelerometer designs. The Q at room temperature is around 10^7 but at $110\,\mathrm{K}$ it drops down to 10^4, and at cryogenic temperatures ($\sim$20 K) it is roughly 10^3 [2]. This drop in Q would result in a lower sensitivity and performance for the system.Current gravitational wave detectors operate at room temperature, however, future detectors will operate at cryogenic temperatures, roughly at or below 20 K [4, 5], to minimize thermal noise. Silicon has demonstrated a high Q-factor across both room and cryogenic temperatures, roughly 5 orders of magnitude higher than fused silica at temperatures from 5 K to 50 K [2]. The Q value for silicon from 10 K to room temperature is between 10^7 and 10^8 [2, 3], which suggests it will be promising for accelerometers working at cryogenic temperatures and for fabrication.

2.2 Mechanical resonator designs

Two designs have been developed and will be fabricated using silicon to operate as compact optomechanical accelerometers that operate compatibly with cryogenic and vacuum environments.

The first design is shown in Figure 2.1a. We call this model the pendulum resonator. This design is based on the Watt-linkage geometry [20, 21] under gravitational restoring force, which was adjusted into an inertial sensor by placing the flexures closer together [22, 23], also known as the folded pendulum. Larger variations of this device have shown promising low frequencies and noise floors [24]. The advantages of this design revolve around the large size of the test mass,

its compactness, and the positioning of the flexures. The location where the flexures connect to the test mass is the most delicate and intricate part of this design. The test mass is suspended across two ends, one by a flexure acting as a "regular" pendulum and another flexure acting as an "inverted" pendulum, acting opposing to each other. The gravity-restoring force of the non-inverted pendulum is balanced by the inverted pendulum's anti-spring gravitational force, which results in less force being needed to displace the test mass. Our version of the pendulum resonator is roughly 30 mm$\times$30 mm with a thickness of 380 μm. This design has a total mass of 0.71 g with the test mass being roughly 0.47 g, and it is supported by two flexures with a thickness of roughly 141 μm.

The second design shown in Figure 2.1b, which we call the parallelogram resonator, is a compact variation of a fully monolithic, dual flexure optomechanical accelerometer developed by Guzman et al. [25] where the two flexures are parallel to each other and equal in size. This design is interesting due to the characteristics of the flexures. The thickness, the length, and the separation of the flexures are what primarily alter and define the fundamental frequency and higher-order modes. Our version of the parallelogram resonator is roughly 15 mm$\times$10 mm with a thickness of 280 μm [18, 17]. This design has a total mass of 72.5 mg with the test mass being roughly 5.4 mg, and it is supported by two flexures with a thickness of roughly 120 μm. The work on these resonators was done in collaboration with Andrea Nelson, Dr. Adam Hines, and Dr. Felipe Guzmán.

Because the pendulum resonator has a lower fundamental frequency with a large test mass, it will be more sensitive for measuring motion, although it will not be able to accurately measure motions that are too fast, shown in Figure 1.1. Oppositely, since the parallelogram resonator has a higher fundamental frequency and smaller test mass it will function better for measuring fast motion.

A model for a fused silica version of the pendulum resonator was also designed, it is shown in Figure 2.2. This version of the pendulum resonator used an earlier design variation of the pendulum design where the flexures were made to flow into a thinner size toward the ends. The thinner ends in this design was influenced by a larger design done in [24, 23] where resonance reached below 1

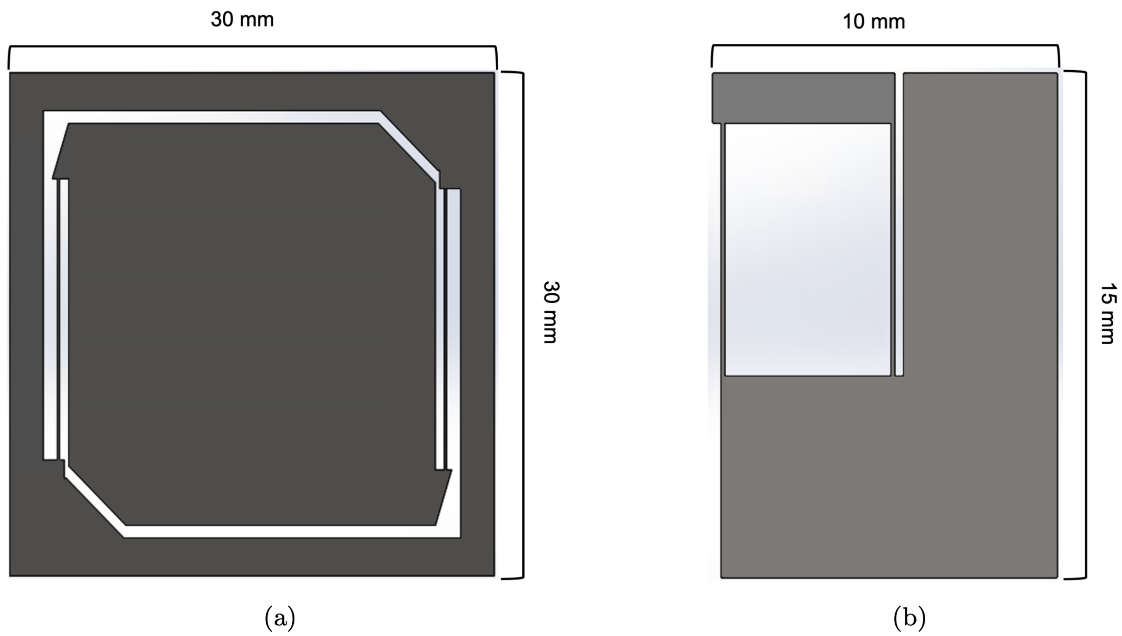

Figure 2.1: (a) Geometry of our silicon pendulum resonator generated in Solidworks. This version of the resonator has overall dimensions of $30\,\mathrm{mm}\times 30\,\mathrm{mm}\times 380\,\mu\mathrm{m}$, and a mass of 0.71 g. The test mass is roughly 0.47 g and is supported by two flexures with a thickness of roughly 141 μm. and (b) Geometry of our silicon parallelogram resonator generated in Solidworks. This version of the resonator has overall dimensions of $15\,\mathrm{mm}\times 10\,\mathrm{mm}\times 280\,\mu\mathrm{m}$, and a mass of 72.5 mg. The test mass is roughly 5.4 mg and is supported by two flexures with a thickness of roughly 120 μm. From these models, we can calculate the mechanical properties of the resonators including the fundamental frequency and maximum stress.

Hz. This version is 30 mm×30 mm and has a thickness of 500 μm. This design has a total mass of 0.95 g with the test mass being roughly 0.59 g, and it is supported by two flexures with a thickness of roughly 95 μm.

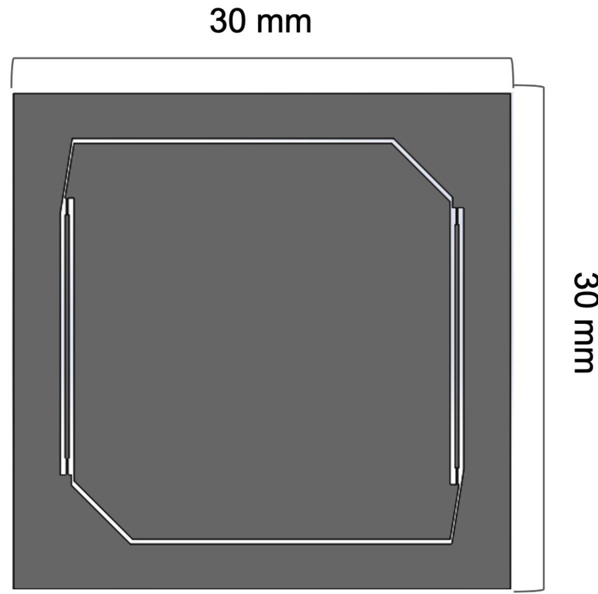

Figure 2.2: Geometry of our fused silica optomechanical pendulum resonator generated in Solidworks. From this model, we can calculate the mechanical properties of our resonator including the fundamental frequency and maximum stress. This version of the resonator has overall dimensions of 30 mm×30 mm×500 μm, and a mass of 0.95 g. The test mass is roughly 0.59 g and is supported by two flexures with a thickness of roughly 95 μm at the thinner portions and 235 μm at the thicker portions.

This design was altered after results obtained through initial tests mentioned in Section 3.3 due to the fragility of the thin sections in the flexures and because the test mass was too close to the frame wall.

2.3 Modeling and analysis

The fundamental frequency, motion, and higher-order modes of oscillation are determined by the characteristics of the resonator, particularly the size of the test mass, the thickness of the sample, and the position and length of the flexures. The theoretical resonator models are developed

and analyzed using the multiphysics software Solidworks and COMSOL.

Linear static and modal simulations are run on the models, and we apply loads such as gravity and applied fixed geometry to estimate the fundamental mode as shown in Figure 2.3 and estimate the maximum stress on the resonator as shown in Figure 2.5 to ensure physical integrity. When modeling our devices we take into consideration the limitations of the material used to withstand stress, deform, and break.

Characteristics such as the bending (flexural) strength, yield strength, and tension strength (Young's modulus) are used. For fused silica, the maximum bending strength is roughly 67 MPa, the yield strength is 70 MPa, and the tension resistance strength is 48 MPa. For silicon, the maximum bending strength is between 200-300 MPa, the yield strength is roughly 120 MPa, and the tensile strength is 113 MPa. Since these strength properties each have a different value, we design our models to have the maximum stress on the body comfortably below the property with the lowest strength of the material, in this case, the tensile strength since the bending and yield strength values are much higher than the tensile strength value.

2.4 Fabrication method

The silicon optomechanical resonators are fabricated at Texas A&M University's Aggiefab Nanofabrication Facility. Due to the limitations of the equipment available, we have formulated the following approach for fabrication. A photomask with our designs are manufactured to be used in the photolithography process for fabrication. The photomask for the two designs are shown in Figure 2.6.

The silicon wafer is cut down to fit the size of the resonator that will be developed, as seen in Figure 2.7.

Second, the wafer is cleaned of any debris, and then the silicon is coated in a thin layer of aluminum via E-beam deposition, shown in Figure 2.8. The aluminum on top of the silicon acts as a selective hard mask to protect the un-exposed silicon beneath it throughout the remainder of the fabrication.

A positive photo-resist is applied above the layer of aluminum and spread out evenly via a spin

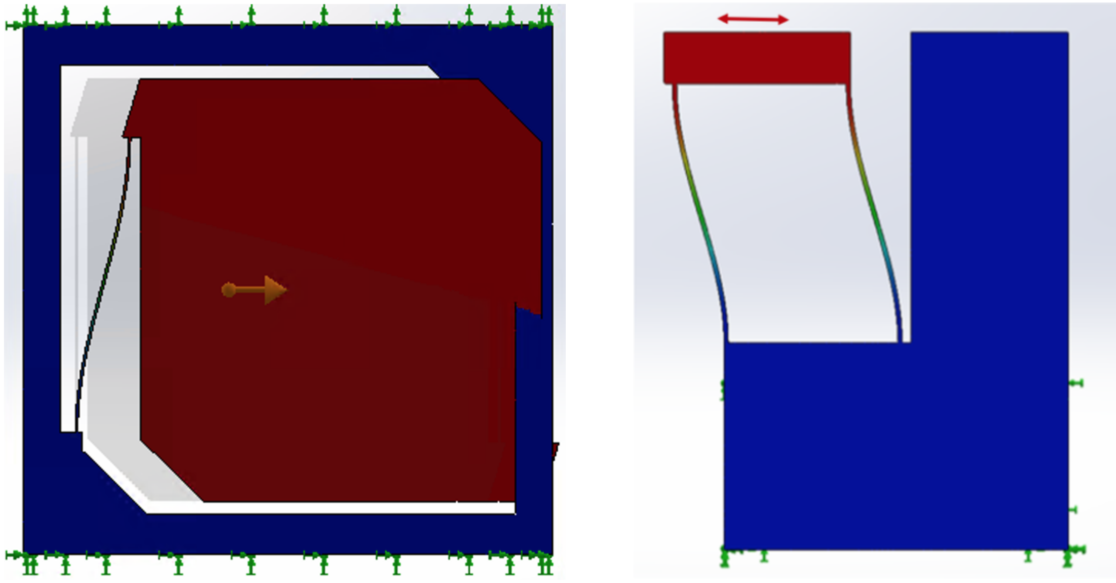

Figure 2.3: A Solidworks simulation of the fundamental mode of the pendulum and parallelogram resonator. The blue color signifies a static area while the red, green, yellow, and orange signify the different amplitudes of the moving parts. The displacement of the test mass in these simulations is exaggerated to show the motion. The expected displacement of the test masses with a force of gravity at $9.8\,m/s^2$ is shown in Figure 2.4

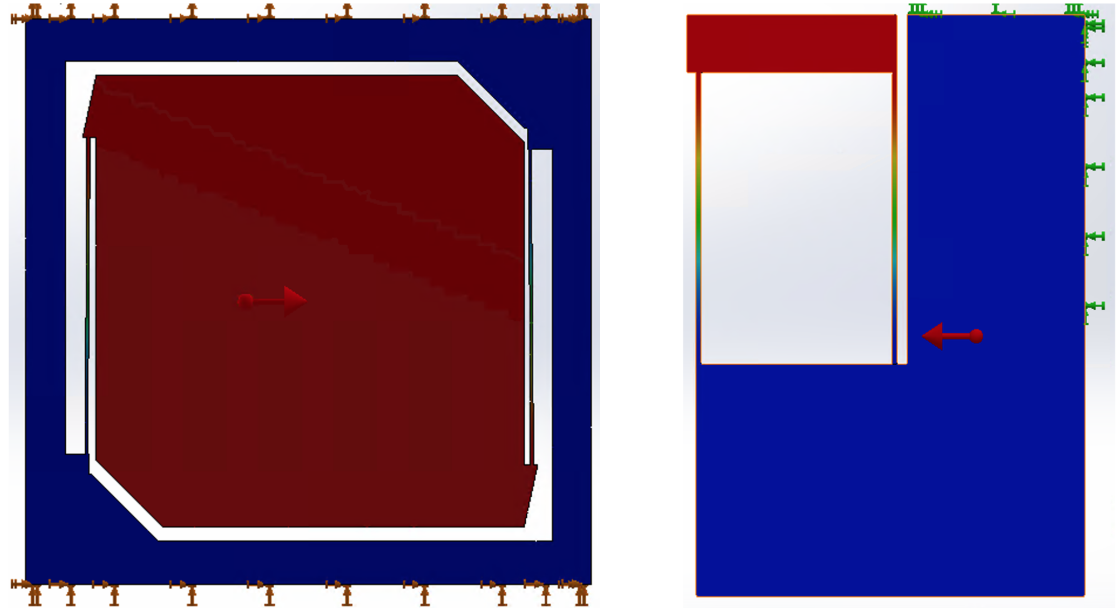

Figure 2.4: A Solidworks simulation of the fundamental mode of the pendulum and parallelogram resonator. The blue color signifies a static area while the red, green, yellow, and orange signify the different amplitudes of the moving parts. The displacement of the test mass in these simulations is to a scale of 1 to show the expected displacement of the test masses with a force of gravity at $9.8\,m/s^2$.

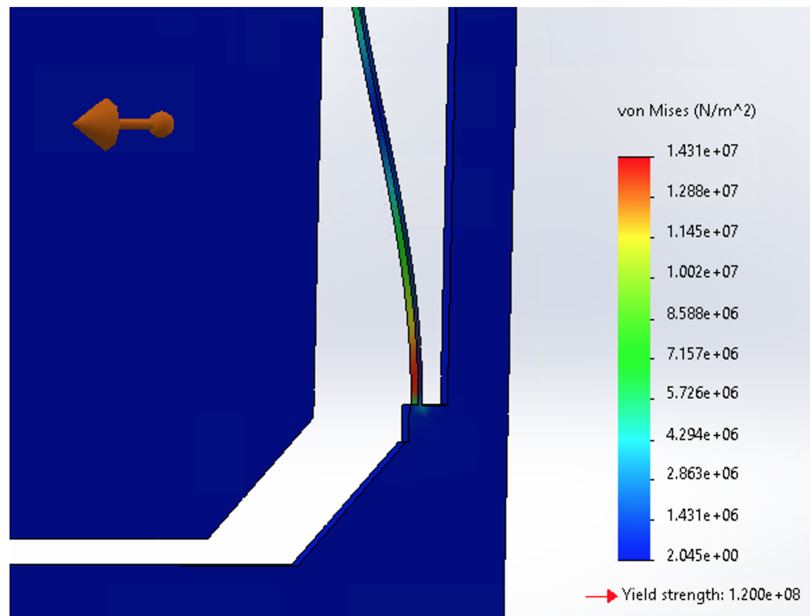

Figure 2.5: A zoomed view of a section from a Solidworks simulation of the stress across the pendulum resonator. The maximum stress on the body will always be where the flexures connect to the frame and test mass. The red signifies the area with the maximum stress while the blue signifies the areas with the minimum stress. As shown on the color bar, the yield strength for silicon is 120 MPa and the maximum stress seen in this simulation is roughly 14.31 MPa.

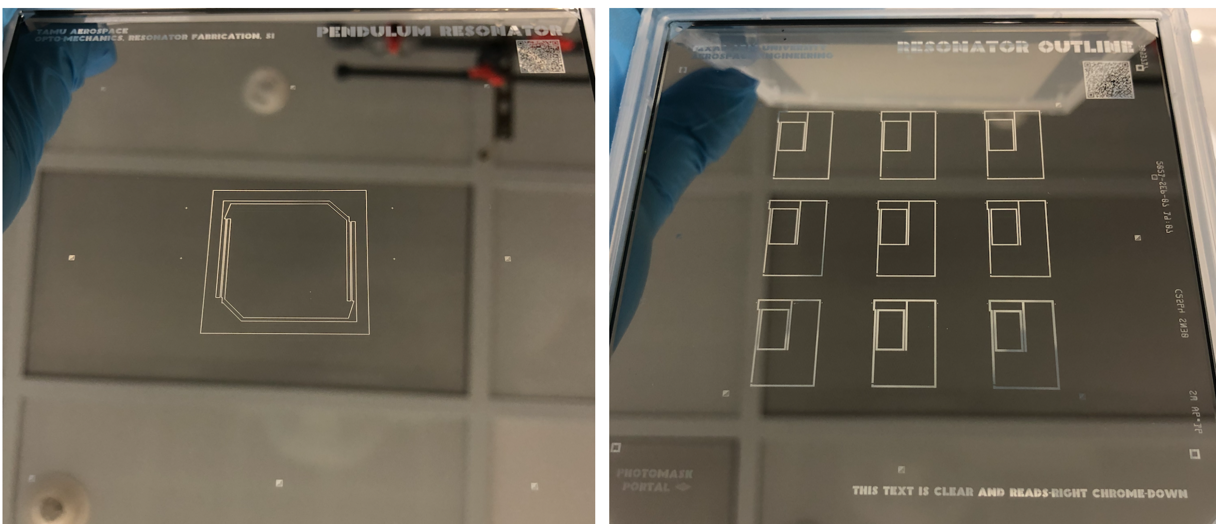

Figure 2.6: The finalized designs of the resonators created in a photomask for performing photolithography. The photomask for the parallelogram has multiple versions of the resonator with varying flexure sizes.

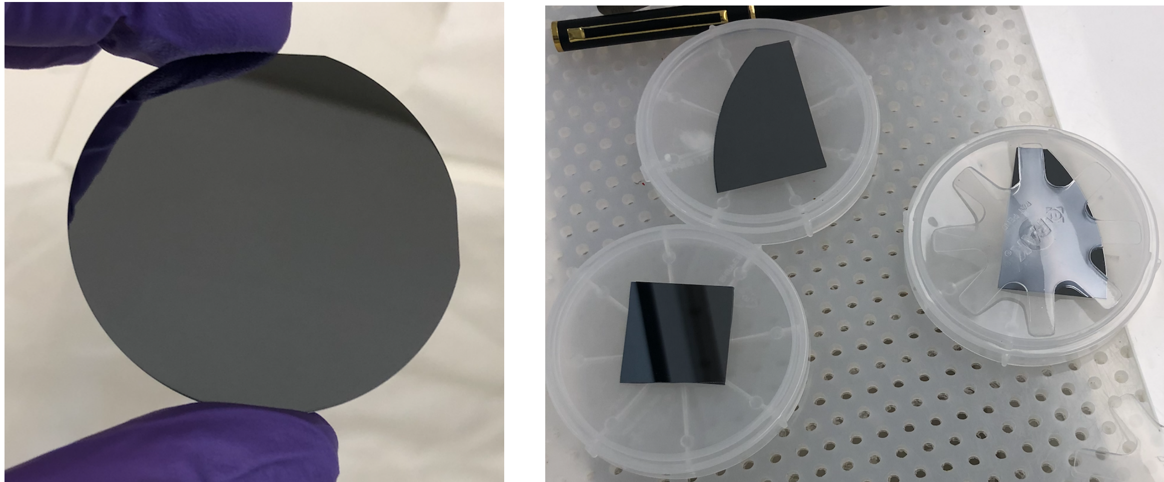

Figure 2.7: The sizes of the silicon wafers we use to fabricate our resonators are often larger than the size of our resonator. By cutting the wafers into smaller pieces we can fabricate multiple resonators using a single wafer.

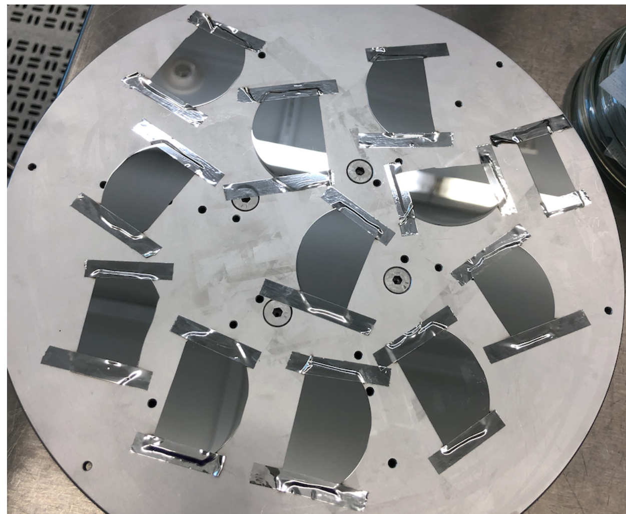

Figure 2.8: The silicon pieces are coated with a layer of aluminum. The aluminum acts as a selective hard mask for the remainder of the fabrication process. This aluminum can be easily removed after fabrication using an aluminum etchant.

coater and soft baked. The layer of photoresist is used to perform lithography. Subsequently, the pattern is exposed onto the photoresist from a photomask using the process of photolithography via an EVG 610 double-sided mask aligner. Areas of the photoresist that are exposed to light through the transparent areas of the photomask during the photolithography step will be weakened and become dissolvable. The weakened areas of photoresist are washed away via a developer, leaving a pattern through the hardened photoresist and above the aluminum, shown in Figure 2.9.

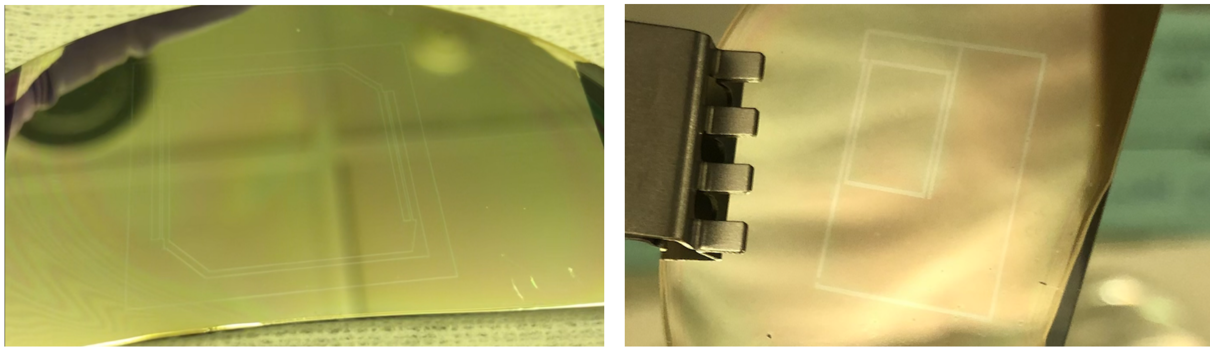

Figure 2.9: A layer of photoresist is applied above the aluminum. As seen in the images above the different colors on the sample represent the varying thickness of the photoresist. When exposed to light the photoresist is selectively weakened and can be washed away using a developer, leaving the lightly shown pattern of the resonator.

An aluminum etchant is used to remove the exposed aluminum in the pattern, leaving the silicon beneath it exposed. The remaining photoresist is then removed, leaving the pattern in the aluminum layer above the silicon, shown in Figure 2.10.

Deep Reactive Ion Etching (DRIE) will be used to etch our pattern via an Oxford Plasmalab 100 ICP RIE system using SF_6 and O_2 gas. This method, known as a Cryo-si etch, uses the formation of plasma to bombard the exposed silicon with ions and etch the silicon away mostly anisotropically. We apply a heat sink paste between the silicon wafer and the carrier wafer to promote thermal conduction since our sample is smaller than 4 inches, shown in Figure 2.11. When the resonator is successfully etched we clean off the heat sink paste residue and the remaining aluminum, leaving only the silicon material.

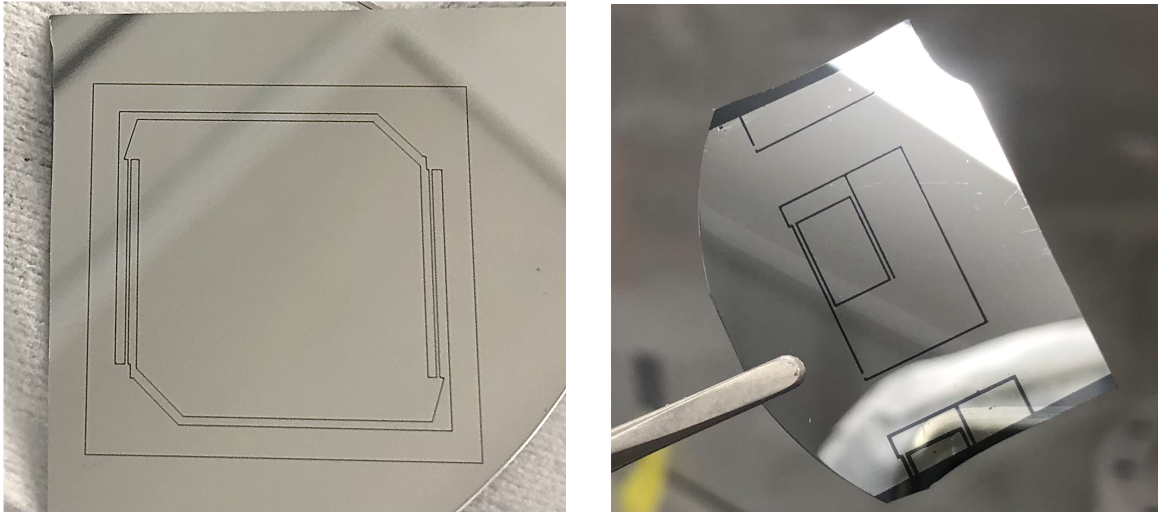

Figure 2.10: Before removing the photoresist, an aluminum etchant is used to remove the exposed areas of aluminum. Once the aluminum is etched we remove any remaining photoresist and are left with a dark pattern in the leftover aluminum. The dark areas are the exposed silicon.

Figure 2.11: To prepare our sample for etching, it needs to be placed onto a carrier wafer. Heat sink paste (shown as dots above) is used to promote anisotropy through thermal conductivity and mount the sample to the carrier wafer so it does not move.

To create the v-grooves onto the parallelogram structure we will be using a KOH etch along the surface of the silicon wafer. This is a wet etch technique that will have to be done before fabricating the rest of the resonator. Si_3N_4 or SiO_2 will be used as a mask to protect the parts of the silicon wafer we do not want etched.

Since the pendulum resonator moves linearly and has the left and right sides of the test mass surrounded by the flexures, we will not be able to etch the v-grooves into the structure itself as the flexures would block the fibers from facing each other. Instead, we will be forming a v-groove on top of the structure using two bare fibers glued together.

2.5 Optical Readout

A Fabry-Pérot (FP) Cavity formed between the tips of two fibers will be used to measure the experimental resonant frequency, Q-factor, and motion of the test mass. The FP cavity is formed between the tips of two single-mode optical fibers cleaved at an angle less than or equal to $0.3°$. The two fibers are placed onto the resonator facing each other, where the primary fiber will lay on the frame and the secondary fiber will lie on the test mass. These fibers can be adjusted and held in place using v-grooves that are either etched into the resonator or formed on top of the resonator by gluing two bare fibers together. A low finesse cavity system is formed when no high reflectivity (HR) coating is applied to the fibers and only the bare fibers are used.

The FP cavity readout method has been used in previous investigations with the larger fused silica resonators used in our lab [15, 16] and will be implemented with the compact resonators. In Figure 2.12 a schematic of the system is shown. Laser light at 1550 nm is used in the system. The laser light goes through a fiber isolator which protects the laser from any reflected light. The laser light then moves into a 50/50 fiber coupler where one end goes to a primary photodetector for power normalization and the second end goes to an optical circulator. The optical circulator is used to further carry the laser light to the cavity formed between the tips of the two fibers and when there is reflected light the circulator will separate the reflected light from the input light and send it to a second photodetector for measurement.

For a low finesse cavity, the voltage reflected from the cavity is proportional to the test mass

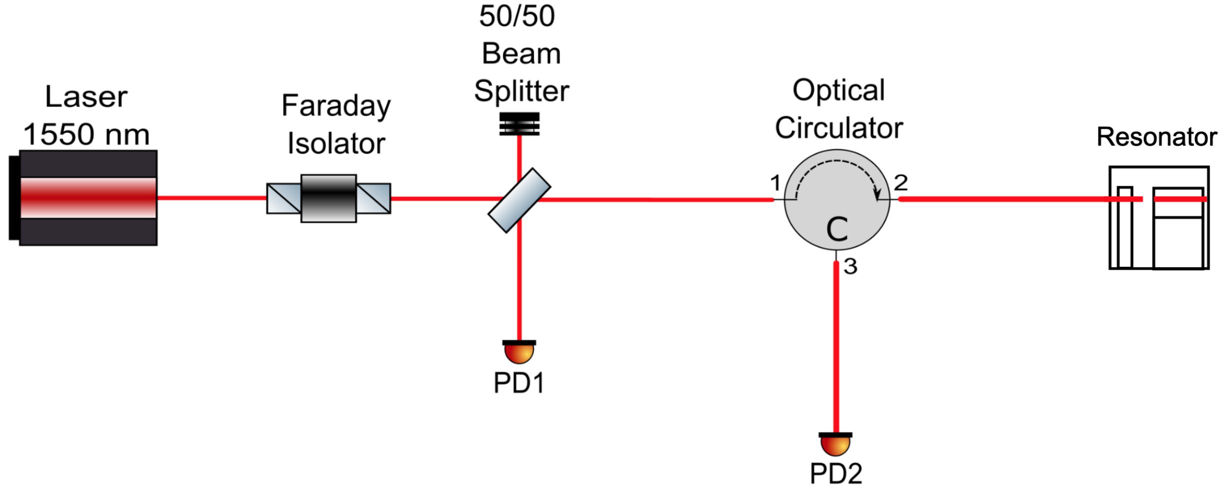

Figure 2.12: A schematic of the components used to create a Fabry-Pérot system. Laser light at 1550 nm is sent through an isolator, which protects the laser from any reflected light. This is followed by a 50/50 fiber split where one half goes through an optical circulator and the other half goes into a primary photodetector for power normalization. The optical circulator carries the laser light to the resonator which is reflected back through the circulator and carried into a secondary photodetector which records the signal.

motion [15]:

$$\delta V = \delta L \frac{\lambda_\mathrm{s}}{L} \frac{\mathrm{d}V}{\mathrm{d}\lambda}\bigg|_{\lambda_\mathrm{s}} \tag{2.1}$$

where λ_s is the laser's wavelength where the cavity sensitivity, $\mathrm{d}V/\mathrm{d}\lambda$, is maximized. L is the cavity length, which is in the order of 60-100 μm, and the voltage as a function of the wavelength is [15]

$$V(\lambda) = A\left(1 - \gamma \frac{1}{1 + \frac{\sin^2 \frac{2\pi L}{\lambda}}{\sin^2 \frac{\pi}{2\mathcal{F}}}}\right) \tag{2.2}$$

where A is the amplitude, γ is the cavity visibility, and $\mathcal{F}$ is the cavity's finesse. The voltage is converted to displacement and, finally, converted to acceleration using the mechanical resonator transfer function, which for $\omega < \omega_0$ is simply $\delta a = \omega_0^2 \delta x$. Previous work [16] using low finesse cavities, $\mathcal{F}$=2, has shown displacement noise levels between 10^{-12} and 10^{-13} m/$\sqrt{\mathrm{Hz}}$ at frequencies around 10 Hz [16]. These noise levels translate to acceleration noise levels between 10^{-7} and 10^{-8} m/s^2/$\sqrt{\mathrm{Hz}}$ for the pendulum resonator. For the parallelogram resonator, the acceleration

noise levels are between 4×10^{-5} and 4×10^{-6} m/s$^2/\sqrt{\mathrm{Hz}}$. Higher displacement sensitivity can be achieved by using high reflectivity coatings on the tips of the fibers and cavity resonance frequency tracking techniques.

Since the pendulum resonator is fabricated from a single piece of silicon wafer and the test mass and flexures are at the center of the structure a mount fabricated from aluminum will be developed so the test mass and flexures can be suspended and move freely. The mount consists of threaded holes along the inner perimeter for the placement of steel alloy ball bearings that will run along the outside frame of the pendulum resonator as seen in Figure 2.13.

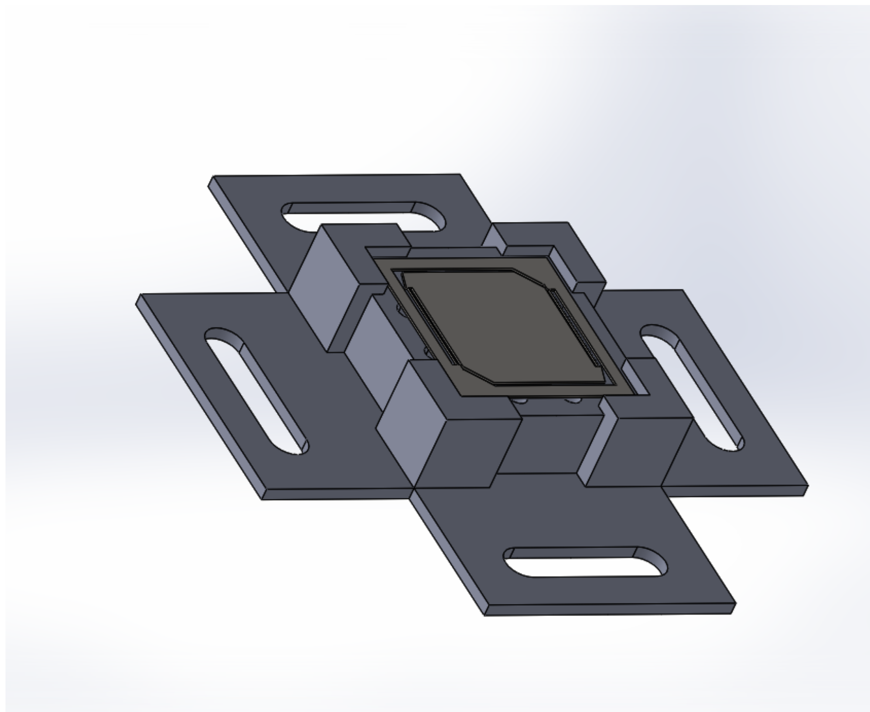

Figure 2.13: A Solidworks assembly of the mount for the pendulum resonator.

3. RESULTS

In this section, we will review the results we have obtained so far regarding the modeling, fabrication, and readout.

3.1 Modeling results

Simulations for the silicon pendulum model give us fundamental frequency geometry of $\omega_0/2\pi$ at roughly 52.44 Hz. For the 380 μm-thick wafer, the fundamental and higher mode frequencies are shown in Table 3.1. We check that the fundamental and higher mode frequencies are largely separated to prevent inter-coupling in the system. The entire mass of the 380 μm-thick model structure is 0.71 g, while the test mass is 0.47 g. A larger test mass allows for better sensitivity due to the inverse relationship between the thermal acceleration noise floor and the mQ product of the resonator [13].

Table 3.1: Theoretical fundamental and higher order modes of the silicon pendulum resonator.

Fundamental Mode	52.4 Hz
2nd Mode	98.6 Hz
3rd Mode	134.5 Hz
4th Mode	252.2 Hz
5th Mode	3.2 kHz

The simulations of the silicon parallelogram model gave us the fundamental frequency, $\omega_0/2\pi$ around 1 kHz. High-order modes are shown in Table 3.2 for a thickness of 280 μm. The entire mass of the 280 μm model structure is 72.5 mg and the test mass is about 5.4 mg.

Using the calculated ω_0 and test mass information we gathered from the theoretical designs, we calculated the expected linear spectral density of displacement and acceleration thermal noise

Table 3.2: Theoretical fundamental and higher order modes of the silicon parallelogram resonator.

Fundamental Mode	1 kHz
2nd Mode	1.1 kHz
3rd Mode	3.6 kHz
4th Mode	3.8 kHz
5th Mode	14.9 kHz

floors [13] for the silicon models at the cryogenic temperature of 20 K and in vacuum. The results of the calculations are shown in Figure 3.1 for the silicon pendulum resonator and Figure 3.2 for the silicon parallelogram resonator.

Simulations for the fused silica pendulum model give us a fundamental frequency geometry of $\omega_0/2\pi$ at roughly 38.75 Hz. For the 500 μm-thick wafer, the fundamental and higher mode frequencies are shown in Table 3.3.

Table 3.3: Theoretical fundamental and higher order modes of the fused silica parallelogram resonator.

Fundamental Mode	39.44 Hz
2nd Mode	126.78 Hz
3rd Mode	153.25 Hz
4th Mode	285.72 Hz
5th Mode	2.9 kHz

The expected linear spectral density of displacement and acceleration thermal noise floor at the room temperature of 293 K and in vacuum was calculated for the fused silica model using the calculated ω_0 and test mass information we gathered. The results of the calculations are shown in Figure 3.3.

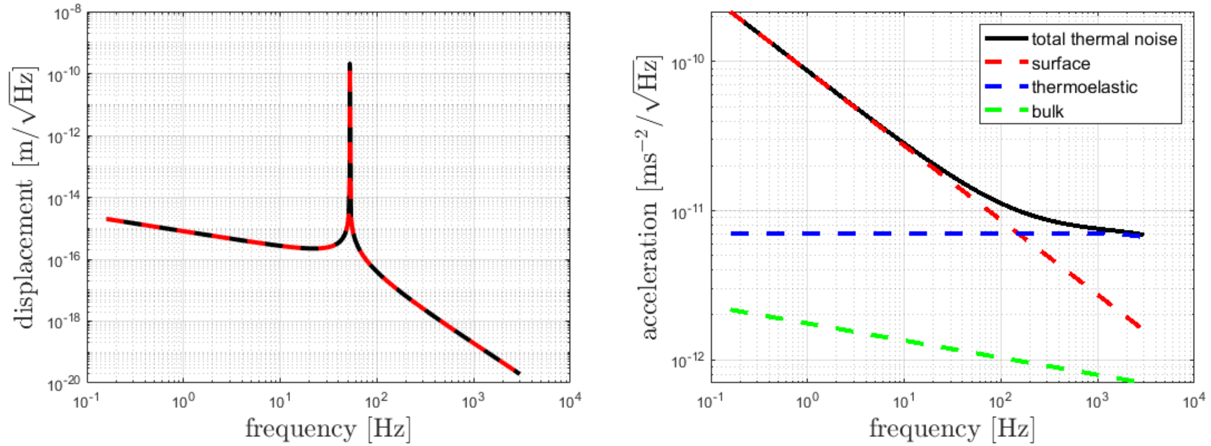

Figure 3.1: (a) Calculated expected linear spectral density of displacement thermal noise floor for a silicon pendulum resonator with a fundamental frequency of 52.4 Hz and 0.47 g test mass at the cryogenic temperature of 20 K and in vacuum, and (b) Calculated expected linear spectral density of acceleration thermal noise for a silicon pendulum resonator with a fundamental frequency of 52.44 Hz and 0.47 g test mass at the cryogenic temperature of 20 K and in vacuum. Also plotted are the contributions from each loss mechanism, from which we can see that surface losses are the dominant noise source for frequencies below resonance followed by thermoelastic losses. The theoretical Q-value for this design is 4.3×10^5.

3.2 Fabrication

3.2.1 Parallelogram resonator

We have successfully fabricated two parallelogram resonators from a 280 μm wafer via the cryo-Si method, which can be seen in Figure 3.4. The process for incorporating the etching of the v-grooves onto the test mass of the parallelogram resonator is currently ongoing.

3.2.2 Pendulum resonator

The fabrication of the pendulum resonator from a 380 μm wafer is ongoing. During initial tests on the fabrication process on the 380 μm wafer, we came across issues with the heat sink paste used to mount the silicon wafer onto the carrier wafer and keep thermal conduction. The heat sink paste has not only caused issues when cleaning our resonators after etching but has gone through the small pieces of the resonator that are fully etched, causing the two walls around the spaces to be stuck together. To overcome the issues with the heat sink paste, we will be applying a thin layer

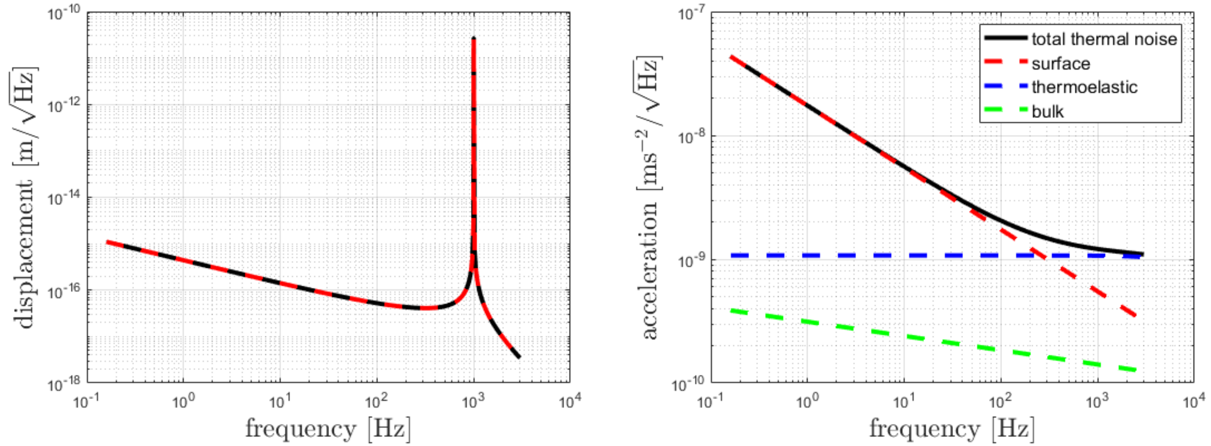

Figure 3.2: (a) Calculated expected linear spectral density of displacement thermal noise floor for a silicon parallelogram resonator with a fundamental frequency of 1 kHz and 5.4 mg test mass at the cryogenic temperature of 20 K and in vacuum, and (b) Calculated expected linear spectral density of acceleration thermal noise for a silicon parallelogram resonator with a fundamental frequency of 1 kHz and 5.4 mg test mass at the cryogenic temperature of 20 K and in vacuum. Also plotted are the contributions from each loss mechanism, from which we can see that surface losses are the dominant noise source for frequencies below resonance followed by thermoelastic losses. The theoretical Q-value for this design is 3.1×10^5

of aluminum beneath the silicon to act as a barrier between the heat sink paste and silicon while still maintaining thermal conduction.

3.3 Fabricated fused silica pendulum resonator

A fabricated fused silica pendulum resonator was tested in air, it is shown in Figure 3.6 compared to the US Nickel.

An in air measurement was done using a flag measurement, the setup is shown in Figure 3.8. A collimated laser was placed above the resonator which layed above a photodetector. The laser beam sat midway across the edge of the test mass and half on the open area. When oscillating the photodetector picks up the oscillations of the test mass by the light being more and less blocked as the test mass moves. The photodetector is connected to a spectrum analyzer to get the frequency. The results from the measurement showed that the fabricated fused silica pendulum resonator displayed a fundamental frequency of around 32 Hz, shown in Figure 3.7. and the Q measurement

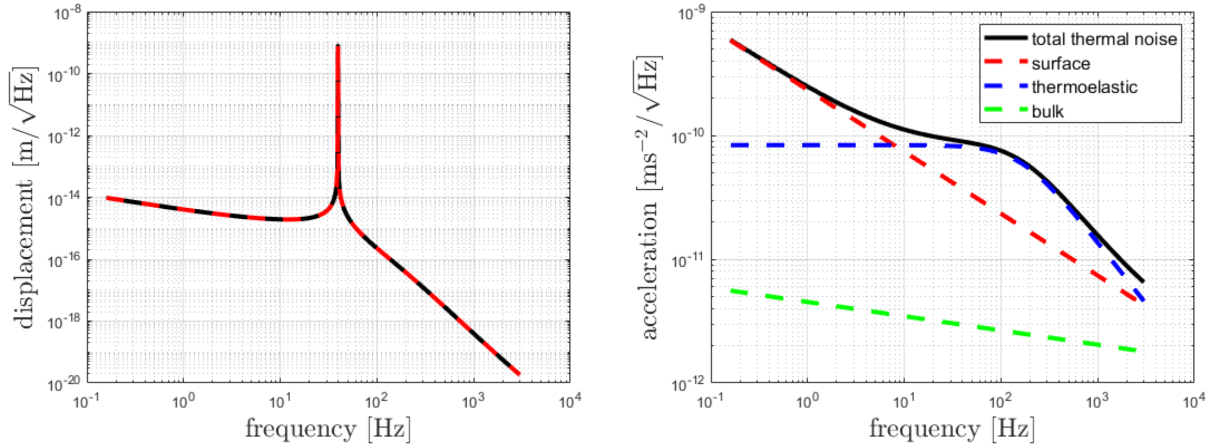

Figure 3.3: (a) Calculated expected linear spectral density of displacement thermal noise floor for a fused silica pendulum resonator with a fundamental frequency of 39.44 Hz and 0.59 g test mass at the room temperature of 293 K and in vacuum, and (b) Calculated expected linear spectral density of acceleration thermal noise for a fused silica pendulum resonator with a fundamental frequency of 39.44 Hz and 0.59 g test mass at the room temperature of 293 K and in vacuum. Also plotted are the contributions from each loss mechanism, from which we can see that surface and thermoelastic losses are the dominant noise source for frequencies below resonance. The theoretical Q-value for this design is 3.0568×10^5.

calculated in air was roughly 2,035.

3.4 Optical Read-out

To understand the Fabry-Pérot set-up, preliminary testing was done using an available fused silica resonator with overall dimensions of 20 mm×17 mm×10 mm and a fundamental frequency around 3 kHz, shown in Figure 3.9.

A low finesse cavity was formed between the tips of two single-mode fibers, where one was left uncoated and the other was coated in high reflectivity coating as shown in Figure 3.10.

A wavelength scan was performed and we measured a cavity length of 108 μm and a finesse of 1.5. Performing a ringdown with this setup will allow us to measure the experimental Q.

The aluminum mount designed for the pendulum resonator has been fabricated and will be used in future testing. It is shown in Figure 3.12.

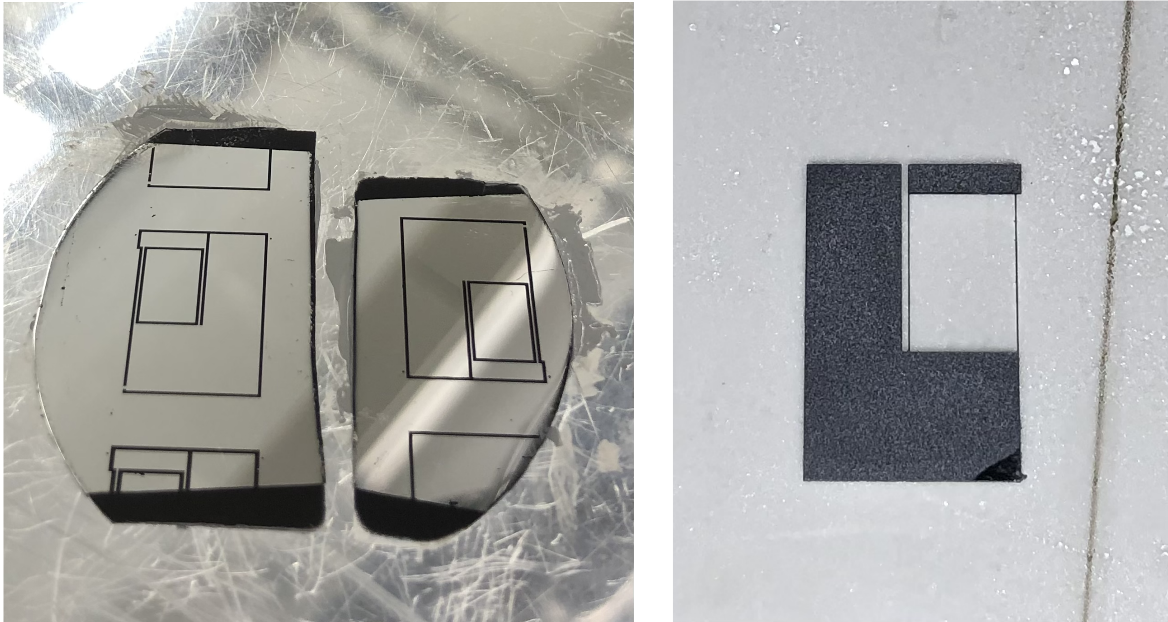

Figure 3.4: (a) The parallelogram resonator pattern is stamped, developed, and has had the aluminum etched away on the patterned sections on two pieces of cut 280 μm silicon wafer. (b) The patterned parallelogram resonator is etched thoroughly through the Cryo-Si process.

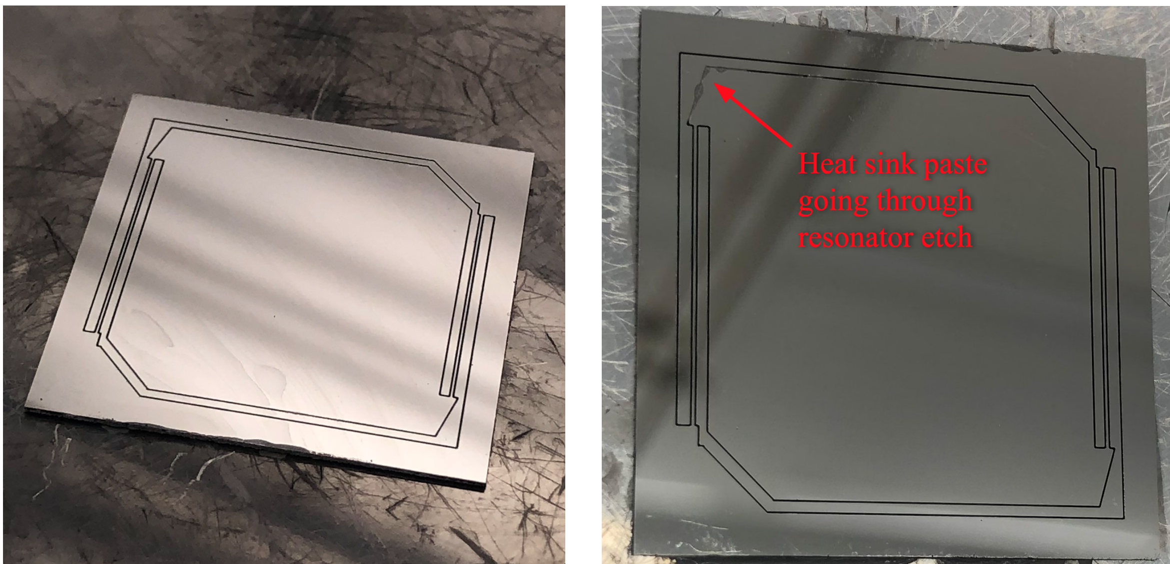

Figure 3.5: (a) The pendulum resonator pattern is stamped, developed, and has had the aluminum etched away on the patterned sections on a piece of 380 μm silicon wafer. (b) The patterned pendulum resonator is partially etched through the Cryo-Si process but has issues with the heat sink paste beneath it.

Figure 3.6: A fully fabricated fused silica pendulum resonator. This model used an earlier design where the flexures thinned out toward the ends. The experimental fundamental frequency for this model was roughly 32 Hz and the Q measurement in air was roughly 2,035.

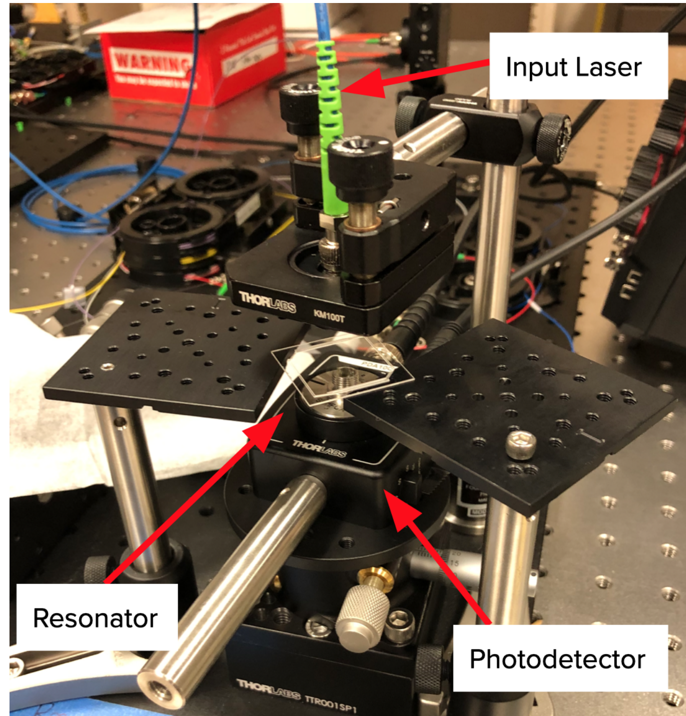

Figure 3.7: An optical flag measurement was utilized to gather a preliminary measurement of the performance of the fully fabricated fused silica pendulum resonator. The experimental fundamental frequency for this model was roughly 32 Hz and the Q measurement in air was roughly 2,035.

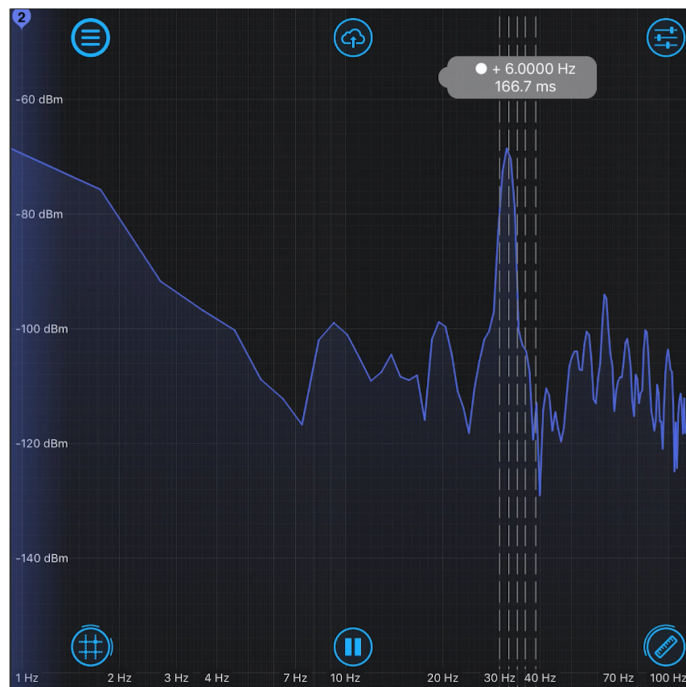

Figure 3.8: The motion recorded from the flag measurement on the fused silica pendulum resonator is shown above. The resonant frequency peak is around 32 Hz.

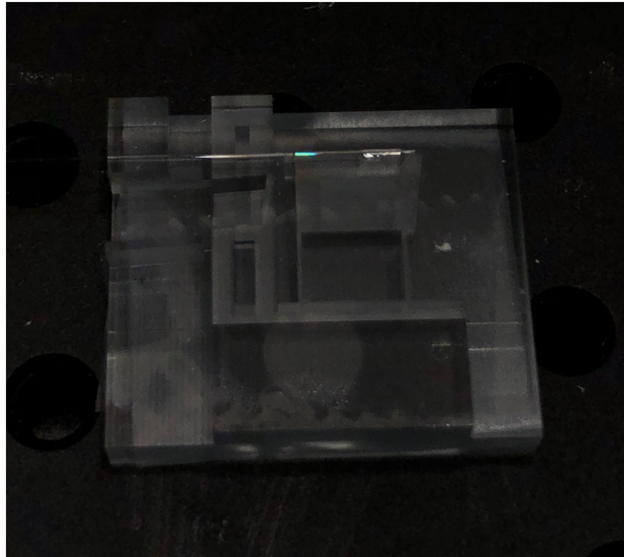

Figure 3.9: A compact fused silica resonator with overall dimensions of 20 mm×17 mm×10 mm and a fundamental frequency of roughly 3 kHz.

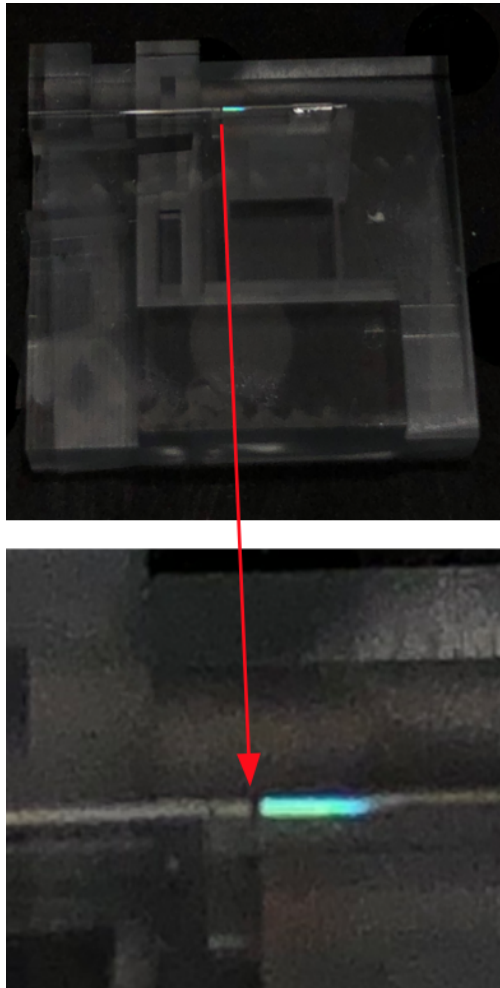

Figure 3.10: A low finesse Fabry-Pérot cavity formed along the top of the fused silica 3 kHz resonator test mass and frame.

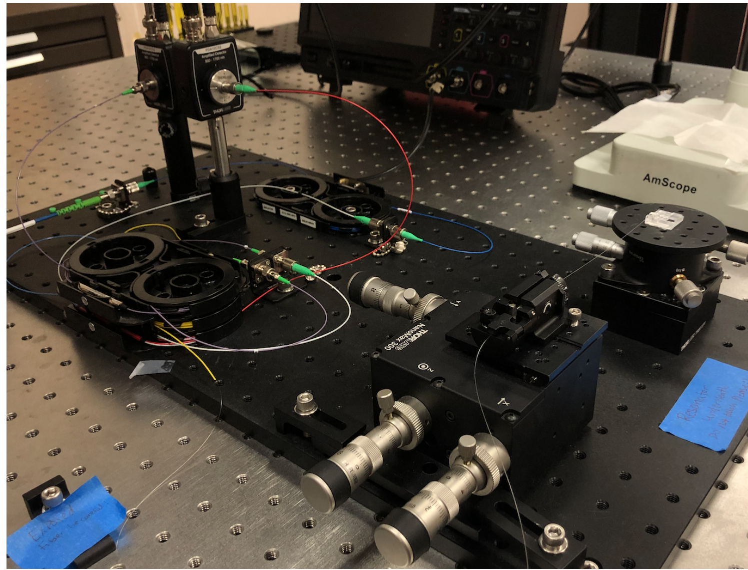

Figure 3.11: The Fabry-Pérot setup attached to the 3 kHz resonator.

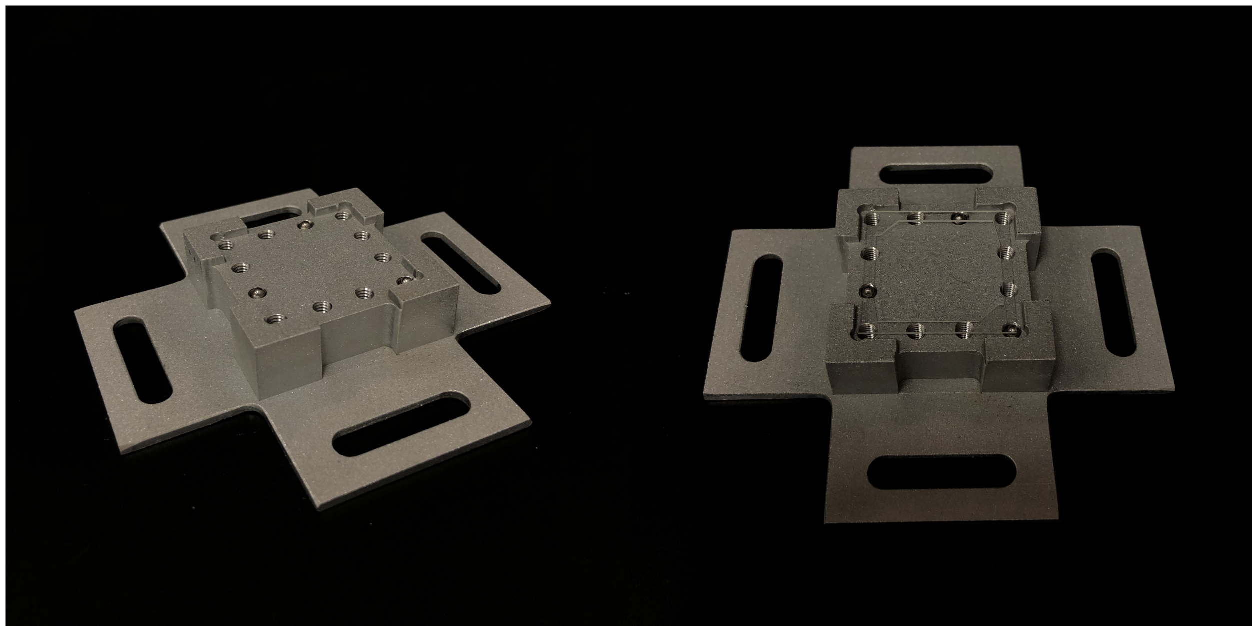

Figure 3.12: The fabricated aluminum mount for the pendulum resonator. The inner perimeter of the mount is lined with threaded holes so ball bearings can be placed. A sample resonator frame is shown sitting on top of them.

4. CONCLUSION

We have developed two silicon compact optomechanical accelerometers that aim to minimize the thermal acceleration noise floor while maintaining a high Q across cryogenic and room temperatures and in vacuum, creating highly sensitive sensors. We have reviewed the promise that compact sensors have displayed in fused silica but have also investigated how silicon will further improve these devices. Silicon is the material chosen for the resonator since it exhibits a high Q-value, and thus reduces the thermal noise limit at low temperatures, as opposed to fused silica that drops rapidly below 250 K. The theoretical values for the 30 mm$\times$30 mm$\times$380 μm pendulum resonator indicate a fundamental resonant mode at 52.4 Hz and Q-value of 4.3×10^5. The theoretical values for the 15 mm$\times$10 mm$\times$280 μm parallelogram resonator are 1 kHz and Q-value of 3.1×10^5.

A fused silica pendulum resonator was designed with overall dimensions of 30 mm$\times$30 mm$\times$500 μm. The theoretical value for the fundamental frequency in this design is 39.44 Hz and a Q of 3.0568×10^5 is expected in vacuum and in room temperature. Experimental testing of a fabricated fused silica pendulum resonator has been done to reveal a fundamental frequency of 32 Hz and a Q of 2,035 in air.

Testing of the Fabry-Pérot cavity readout was completed using a compact fused silica resonator with overal dimensions of 20 mm$\times$17 mm$\times$10 mm with a fundamental frequency around 3 kHz, a cavity length of 108 μm was calculated with a finesse of 1.5.

This thesis discussed the design and fabrication of two silicon compact optomechanical accelerometers, and the foreseen optical read-out to measure the motion of the test masses, the Fabry-Pérot readout.

4.1 Future work

Due to the challenges we have faced with the heat sink paste portion of fabrication, we plan to resolve this issue by adding a layer of aluminum beneath the silicon to act as a barrier between the

silicon and the paste. It is much easier to wipe the heat sink paste off of a large smooth surface and remove the remaining aluminum through an aluminum etchant. Since our pendulum resonator is in the early stages, a v-groove will have to be formed on top of the test mass and across the frame using two bare fibers glued together. This is another difficult task as we have to be careful with the flexures beneath the fibers when cutting them. We will also have to be as precise as possible to ensure the v-grooves are parallel to each other. We will also further investigate the KOH etching process for the v-grooves on the parallelogram resonator. We also plan on developing a process to etch the tips of GE-doped single mode fibers by immersing the tip into a bath of hydrofluoric acid to create an oval cavity in the tip creating a high reflectivity cavity [26]. Finally, we will continue to work on the overall fabrication process for the pendulum and parallelogram resonator. Given a completely fabricated sample, we will experimentally measure the resonators' performance.

REFERENCES

[1] G. Valdes, A. Hines, A. Nelson, Y. Zhang, and F. Guzman, “A characterization method for low-frequency seismic noise in ligo,” *Applied Physics Letters*, vol. 121, no. 23, p. 234102, 2022.

[2] R. Schnabel, M. Britzger, F. Brückner, O. Burmeister, K. Danzmann, J. Duck, T. Eberle, D. Friedrich, H. Luck, M. Mehmet, R. Nawrodt, S. Steinlechner, and B. Willke, “Building blocks for future detectors: Silicon test masses and 1550 nm laser light,” *Journal of Physics: Conference Series*, vol. 228, p. 012029, may 2010.

[3] R. Nawrodt, A. Zimmer, T. Koettig, C. Schwarz, D. Heinert, M. Hudl, R. Neubert, M. Thürk, S. Nietzsche, W. Vodel, *et al.*, “High mechanical q-factor measurements on silicon bulk samples,” in *Journal of Physics: Conference Series*, vol. 122, p. 012008, IOP Publishing, 2008.

[4] T. Akutsu, K. collaboration, *et al.*, “Large-scale cryogenic gravitational-wave telescope in japan: Kagra,” in *Journal of Physics: Conference Series*, vol. 610, p. 012016, IOP Publishing, 2015.

[5] B. Shapiro, R. X. Adhikari, O. Aguiar, E. Bonilla, D. Fan, L. Gan, I. Gomez, S. Khandelwal, B. Lantz, T. MacDonald, *et al.*, “Cryogenically cooled ultra low vibration silicon mirrors for gravitational wave observatories,” *Cryogenics*, vol. 81, pp. 83–92, 2017.

[6] Y. Dong, P. Zwahlen, A.-M. Nguyen, F. Rudolf, and J.-M. Stauffer, “High performance inertial navigation grade sigma-delta mems accelerometer,” in *IEEE/ION Position, Location and Navigation Symposium*, pp. 32–36, IEEE, 2010.

[7] A. Bertolini, R. DeSalvo, F. Fidecaro, M. Francesconi, S. Marka, V. Sannibale, D. Simonetti, A. Takamori, and H. Tariq, “Readout system and predicted performance of a low-noise low-frequency horizontal accelerometer,” *Nuclear Instruments and Methods in Physics Research Section A: Accelerators, Spectrometers, Detectors and Associated Equipment*, vol. 564, no. 1, pp. 579–586, 2006.

[8] R. Middlemiss, A. Samarelli, D. Paul, J. Hough, S. Rowan, and G. Hammond, "Measurement of the earth tides with a mems gravimeter," *Nature*, vol. 531, no. 7596, pp. 614–617, 2016.

[9] J. N. Schoess, D. K. Arch, W. Yang, C. Cabuz, B. Hocker, B. R. Johnson, and M. L. Wilson, "Mems sensing and control: An aerospace perspective," in *Smart Structures and Materials 2000: Smart Electronics and MEMS*, vol. 3990, pp. 22–27, SPIE, 2000.

[10] Z. Li, W. J. Wu, P. P. Zheng, J. Q. Liu, J. Fan, and L. C. Tu, "Novel capacitive sensing system design of a microelectromechanical systems accelerometer for gravity measurement applications," *Micromachines*, vol. 7, no. 9, p. 167, 2016.

[11] D. Davis, J. S. Areeda, B. K. Berger, R. Bruntz, A. Effler, R. Essick, R. Fisher, P. Godwin, E. Goetz, A. Helmling-Cornell, *et al.*, "Ligo detector characterization in the second and third observing runs," *Classical and Quantum Gravity*, vol. 38, no. 13, p. 135014, 2021.

[12] A. Hines, *DEVELOPMENT OF AN OPTOMECHANICAL RESONATOR FOR LOW-FREQUENCY ACCELERATION SENSING*. PhD thesis, Texas A&M University, 2022.

[13] A. Hines, L. Richardson, H. Wisniewski, and F. Guzman, "Optomechanical inertial sensors," *Applied optics*, vol. 59, no. 22, pp. G167–G174, 2020.

[14] P. R. Saulson, "Thermal noise in mechanical experiments," *Physical Review D*, vol. 42, no. 8, p. 2437, 1990.

[15] F. Guzmán Cervantes, L. Kumanchik, J. Pratt, and J. M. Taylor, "High sensitivity optomechanical reference accelerometer over 10 khz," *Applied Physics Letters*, vol. 104, no. 22, p. 221111, 2014.

[16] F. Guzman, L. M. Kumanchik, R. Spannagel, and C. Braxmaier, "Compact fully monolithic optomechanical accelerometer," *arXiv preprint arXiv:1811.01049*, 2018.

[17] A. Nelson and F. Guzman, "Compact optomechanical inertial sensors with fused silicia and si-based resonators," in *Optical and Quantum Sensing and Precision Metrology II*, vol. 12016, pp. 91–96, SPIE, 2022.

[18] A. Nelson and F. Guzman, “Micro-fabrication of si-based optomechanical inertial sensors for cryogenic temperatures,” in *Applied Optical Metrology IV*, vol. 11817, pp. 78–83, SPIE, 2021.

[19] B. B. Martinez, A. Nelson, A. Hines, J. P. Mock, G. Valdés, J. Sanjuan, and F. Guzmán, “Modeling, fabrication, and readout of compact optomechanical accelerometers,” in *MOEMS and Miniaturized Systems XXII* (H. Zappe, W. Piyawattanametha, and Y.-H. Park, eds.), vol. 12434, p. 1243404, International Society for Optics and Photonics, SPIE, 2023.

[20] B. Spear, “James watt: The steam engine and the commercialization of patents,” *World Patent Information*, vol. 30, no. 1, pp. 53–58, 2008.

[21] D. G. Blair, J. Liu, E. F. Moghaddam, and L. Ju, “Performance of an ultra low-frequency folded pendulum,” *Physics Letters A*, vol. 193, no. 3, pp. 223–226, 1994.

[22] A. Bertolini, R. DeSalvo, F. Fidecaro, M. Francesconi, S. Marka, V. Sannibale, D. Simonetti, A. Takamori, and H. Tariq, “Mechanical design of a single-axis monolithic accelerometer for advanced seismic attenuation systems,” *Nuclear Instruments and Methods in Physics Research Section A: Accelerators, Spectrometers, Detectors and Associated Equipment*, vol. 556, no. 2, pp. 616–623, 2006.

[23] A. Bertolini, R. DeSalvo, F. Fidecaro, and A. Takamori, “Monolithic folded pendulum accelerometers for seismic monitoring and active isolation systems,” *IEEE transactions on geoscience and remote sensing*, vol. 44, no. 2, pp. 273–276, 2006.

[24] N. de Gaay Fortman, “Instruments for seismic isolation: Improving performance of advanced displacement and inertial sensors for active suppression of seismic noise in gravitational wave detectors,” 2019.

[25] F. Guzman, L. M. Kumanchik, R. Spannagel, and C. Braxmaier, “Compact fully monolithic optomechanical accelerometer,” 2018.

[26] L. M. Soares, J. D. Lopez, R. C. Allil, A. Dante, and M. M. Werneck, "Fiber-optic magnetic field sensors based on in-fiber fabry-pérot interferometers," in *Latin America Optics and Photonics Conference*, pp. W1C–7, Optica Publishing Group, 2022.